# Magnetosphere preconditioning under northward IMF: Evidence from the study of coronal mass ejection and corotating interaction region geoeffectiveness

B. Lavraud,[1] M. F. Thomsen,[1] J. E. Borovsky,[1] M. H. Denton,[1] and T. I. Pulkkinen[1]

[1] Motivated by recent observations and simulations of the formation of a cold and dense plasma sheet in the tail of the magnetosphere under northward interplanetary magnetic field (IMF) and of the direct influence of the plasma sheet density on the ring current strength, this paper aims at (1) highlighting how the coupling of these effects may lead to a preconditioning of the magnetosphere under northward IMF and (2) performing first tests of the validity of this hypothesis. We have analyzed superposed epoch time series of various parameters to investigate the response of the magnetosphere (as indicated by the $Dst$ index) to the passage of coronal mass ejections (CMEs) and corotating interaction regions (CIRs). We first focused on the difference between the measured $Dst$ signature and that predicted by a semiempirical $Dst$ model. For both CME- and CIR-driven storms the superposed epoch results show that the model $Dst$ predictions tend to underestimate the actual storm strength (by up to $10-30\%$) for events that are preceded by a substantial interval of northward IMF, as opposed to those with no such preceding northward IMF. We also analyzed Los Alamos geosynchronous spacecraft data for these events. The average density and temperature measured at storm onset are substantially higher and slightly lower, respectively, for the cases with preceding northward IMF intervals. These results suggest that solar wind structures may be more geoeffective if preceded by a northward IMF interval and they are consistent with the hypothesis of a preconditioning by a cold, dense plasma sheet. A colder and denser plasma sheet may lead to a stronger ring current when that plasma is convected inward during the main phase of an ensuing storm.

## 1. Introduction

[2] The investigation of the geoeffectiveness of coronal mass ejections (CMEs) and corotating interaction regions (CIRs) has recently gained much interest in the context of space weather studies and the upcoming launch of missions aimed at studying such structures and their impact on Earth [*Zhang and Burlaga*, 1988; *Gosling et al.*, 1991; *Gosling*, 1993; *Kamide et al.*, 1998; *Gonzalez et al.*, 2002a, 2002b; *Cane and Richardson*, 2003; *Li and Luhmann*, 2004; *Wu and Lepping*, 2002, 2005; *Borovsky and Steinberg*, 2006]. It is known that a portion of CMEs have a well-defined embedded magnetic flux rope-like structure; these are called magnetic clouds. Magnetic clouds often have a bipolar structure in their magnetic field. When the orientation of their main axis has a significant horizontal component, they are usually referred to as north-south or south-north polarity magnetic clouds.

Magnetic clouds are often geoeffective structures as they usually possess a relatively strong and persistent southward magnetic field component either in the leading or trailing portion of the structure. However, the geoeffectiveness of CMEs can also be driven by the preceding sheath region of the CMEs owing to its compressed and fluctuating nature [*Gosling et al.*, 1991; *Huttunen et al.*, 2002]. CIRs are similarly important geoeffective structures [*Kamide et al.*, 1998; *Gonzalez et al.*, 2002b; *Borovsky and Steinberg*, 2006; *Denton et al.*, 2006] as the increased speed during such events is often accompanied by a southward component of the interplanetary magnetic field (IMF), leading to a strong coupling through a large solar wind electric field imposed on the magnetosphere. The geoeffectiveness of solar wind structures (either CMEs or CIRs) is thus to first order attributable to the presence of a large solar wind electric field and a large dynamic pressure [e.g., *Burton et al.*, 1975; *Akasofu*, 1981].

[3] A commonly used index for assessment of geomagnetic activity is $Dst$, which is a measure of the strength of the ring current. $Dst$ has been shown to correlate strongly with the magnitude of the solar wind electric field and dynamic

---

[1]Space Science and Applications, Los Alamos National Laboratory, Los Alamos, New Mexico, USA.

pressure. These correlations allowed *Burton et al.* [1975] to construct a semiempirical model of the *Dst* response based on inputs from the solar wind parameters. This predictive model was further modified and adapted successively by *O'Brien and McPherron* [2000] and *Wang et al.* [2003]. It is known that contributions to *Dst* come from other (e.g., tail) current systems as well [e.g., *Hakkinen et al.*, 2003; *Ganushkina et al.*, 2004]. These currents may not be separated in the present study. Their contribution, however, may be viewed as part of the global geoeffectiveness of the events under consideration here.

[4] From the study of the statistical significance of the difference between their predicted and the measured *Dst*, *O'Brien and McPherron* [2000] concluded that the errors in their model were caused by a few rather than many sources. An obvious source of errors is that of the measurements themselves [*O'Brien and McPherron*, 2000]. In addition, because of the sole dependence of the model on the solar wind electric field and dynamic pressure, the effects of other operative physical processes ought to constitute additional sources of discrepancy. One such mechanism investigated here is a preconditioning of the magnetosphere under northward IMF; i.e., the possibility that the magnetosphere configures itself in a specific state as a function of the properties of the preceding solar wind conditions, which in turn may affect the strength of ensuing storms. Of particular importance in this context is the formation of a colder and denser plasma sheet during northward IMF [*Terasawa et al.*, 1997; *Fujimoto et al.*, 1998]. Both observations [*Borovsky et al.*, 1997; *Thomsen et al.*, 1998] and modeling efforts [*Jordanova et al.*, 1998; *Kozyra et al.*, 1998] have shown evidence for the role of the plasma sheet density in storm-time ring current strength, with larger plasma sheet density leading to larger negative *Dst* excursions. A lower plasma sheet temperature may add to the ring current strength as colder populations may convect deeper Earthward than their hotter counterpart [*Ebihara and Ejiri*, 2000]. In this paper we argue that the formation of a cold, dense plasma sheet (CDPS) may lead to an enhanced *Dst* during the main phase of a storm as that denser plasma is being pushed inward during the strong convection associated with the storm main phase.

[5] A number of studies have investigated a possible dependence of CMEs geoeffectiveness on the polarity of magnetic clouds [*Zhang and Burlaga*, 1988; *Fenrich and Luhmann*, 1998; *Li and Luhmann*, 2004; *Wu and Lepping*, 2002, 2005]. However, a relation between CME magnetic polarity and their absolute geoeffectiveness (in terms of *Dst* in particular) has not been fully pinned down. This is in part due to the lack of extended databases of magnetic clouds, i.e., only a subset of all CMEs. It is further complicated by the common presence of a sheath ahead of the CME itself, which often is the first geoeffective part of CMEs [*Gosling et al.*, 1991]. Periods of calms (defined as a *Kp* index lower than $1^+$ for at least 6 hours) before CIR-driven storms have been noted and investigated recently by *Borovsky and Steinberg* [2006]. They showed that such calm periods occur more frequently prior to CIR-driven storms than during more typical solar wind conditions. In their discussion, they suggested that such periods of calm may lead to a preconditioning of the magnetosphere by, in particular, (1) a possible mass loading after the buildup of a dense plasmasphere during quiet (low *Kp*) intervals, and (2) the formation of a cold and dense plasma sheet, in response to presumably northward IMF (as also suggested by *Thomsen et al.* [2003]).

[6] There is ample evidence that both double high-latitude reconnection [*Song and Russell*, 1992; *Øieroset et al.*, 2005; *Li et al.*, 2005; *Lavraud et al.*, 2005a, 2006] and the Kelvin-Helmholtz instability [*Fujimoto et al.*, 1998; *Hasegawa et al.*, 2004] may participate in the formation of the cold, dense plasma sheet (CDPS) under northward IMF. Here we do not focus on the relative importance of these processes, we only rely on the fact that the presence of the CDPS following extended periods of northward IMF is well established [e.g., *Terasawa et al.*, 1997] and that this material has access to the inner magnetosphere under certain conditions [*Thomsen et al.*, 2003; *Lavraud et al.*, 2005b].

[7] Any signature of the dependence of storm strength on the preceding solar wind conditions (IMF direction in particular) is necessarily embedded in the measured *Dst* trend. Primarily, *Dst* responds to coupling through the solar wind electric field and dynamic pressure. Therefore, to assess the role of secondary effects such as a preconditioning of the magnetosphere under northward IMF, one must either (1) compare the magnetospheric response of CMEs or CIRs which have similar solar wind characteristics apart from their magnetic structure (resulting in a limited number of suitable events, if any) or (2) statistically compare the actual magnetospheric response to that predicted by models which are developed to take into account the effects of the solar wind electric field and dynamic pressure. In the latter case, systematic differences observed between different sets of storms selected for specific preceding IMF conditions can be interpreted to be due to other coupling processes. This is the approach we use in the present study. In addition, we use in situ measurements of the density and temperature of the nightside plasma sheet to assess the role of the formation of a CDPS as a preconditioning mechanism.

[8] We first describe the data, the *Dst* model and the event selection criteria in section 2. In section 3 we show and discuss the results. These primarily pertain to the difference observed between the measured and modeled *Dst*, as a function of preceding IMF conditions. The connection to plasma sheet density and temperature is then documented with measurements of the densities and temperatures in the nightside sector of geosynchronous orbit. Potential limiting factors to this mechanism are discussed in section 3.5. We draw our conclusions in section 4.

## 2. Data, *Dst* Model, and Event Selection

### 2.1. Data

[9] In this study, we use solar wind data from the OMNI-2 data set [*King and Papitashvili*, 2005]. This data set extends from 1963 with hourly averages of solar wind data from various solar wind monitors. Lag times from the observing spacecraft to Earth are already applied in the data set. The OMNI-2 data set has the same time resolution as the *Dst* index and therefore was used by *O'Brien and McPherron* [2000] for the construction of the *Dst* model described below. *Dst* and *Kp* data are also taken from the OMNI-2 data set. The GSM coordinates are used throughout the paper.

[10] We also make use of measurements from the Los Alamos National Laboratory MPA (Magnetospheric Plasma Analyzer) instruments onboard geosynchronous satellites.

The MPA instruments are electrostatic analyzers. They measure the three-dimensional energy-per-charge distributions of both ions and electrons. Here we only utilize measurements of the ion density and temperature, which are calculated for the energy range [100–45000] eV [*Thomsen et al.*, 1999] (all ions are assumed to be protons). The reader is referred to *Bame et al.* [1993] and *McComas et al.* [1993] for detailed description of the MPA instruments. For the current study, data are taken from six different satellites in geosynchronous orbit covering the period of interest between 1994 and 2003.

## 2.2. *Dst* Model

[11] The *Dst* model used in this study comes from *Wang et al.* [2003]. It is a modified version of the *O'Brien and McPherron* [2000] model that is designed to better represent the *Dst* dependence on the solar wind dynamic pressure. These models are based on that originally developed by *Burton et al.* [1975].

[12] The measured *Dst* index is known to have a substantial contribution coming from the magnetopause current system (i.e., the currents over the entire magnetopause induce deflections of the magnetic field at the surface of the Earth that are necessarily included as part of the *Dst* index). This contribution ought to be removed prior to analyzing *Dst* as an actual index representing the strength of the intramagnetospheric currents, and, in particular, of the ring current itself. Contribution from the magnetopause currents mainly depends on the solar wind dynamic pressure and, in the model used here, is given by [e.g., *O'Brien and McPherron*, 2000]:

$$Dst^* = Dst - 7.26\sqrt{P_{ram}} + 11 \qquad (1)$$

where $P_{ram}$ is the solar wind dynamic pressure, *Dst* is the measured index and *Dst** is that corrected for the contribution of magnetopause currents.

[13] In the models, *Dst** variations are assumed to be the result of an injection term (first right hand term in equation (2)) and a decay term (second right hand term in equation (2), where $\tau$ is a decay timescale in hours):

$$\frac{d}{dt}Dst^*(t) = Q(t) - \frac{Dst^*(t)}{\tau} \qquad (2)$$

The statistical analysis of the response of *Dst** to solar wind parameters allowed *Burton et al.* [1975], and later *O'Brien and McPherron* [2000] and *Wang et al.* [2003], to find the functional dependence of each term in the *Dst** variations as a function of the solar wind electric field ($E_y$ or $VBz$ parameter, in mV/m) and the solar wind dynamic pressure ($P_{ram}$ in nPa). For the results shown in the next sections, we used the parameterization from *Wang et al.* [2003]. For the injection term $Q$ (nT h$^{-1}$), this parameterization is as follows:

$$Q = 0 \qquad VBz \leq 0.49 \text{ mV/m} \qquad (3a)$$

$$Q = -4.4(VBz - 0.49)\left(\frac{P_{ram}}{P_0}\right)^{\gamma} \qquad VBz > 0.49 \text{ mV/m} \quad (3b)$$

where the best fit parameters $P_0$ and $\gamma$ were found to be 3.0 nPa and 0.2, respectively. The decay timescale $\tau$ (in hours) from equation (2) has the following parameterization:

$$\tau = 8.70e^{6.66/(6.04+P_{ram})} \qquad Bz \geq 0 \text{ nT} \qquad (4a)$$

$$\tau = 2.40e^{9.74/(4.69+VBz)} \qquad Bz < 0 \text{ nT} \qquad (4b)$$

The implementation of this *Dst** model thus requires that solar wind data be available. In our analysis, from a given start time forward, the *Dst** index is calculated at time $t + \Delta t$ ($\Delta t$ is 1 hour) by straight integration of equation (2) using the solar wind data at time $t$ as input. In this paper, we will only show *Dst** values, i.e., both model and measured *Dst* at time $t$ are corrected for the magnetopause current contribution using equation (1). The results shown in this paper also hold when using the *O'Brien and McPherron* [2000] parameterization instead of that of *Wang et al.* [2003].

## 2.3. Event Selection

[14] We study both CME- and CIR-driven storms. The list of CMEs used in this study comes from *Cane and Richardson* [2003]. The list of CIRs we used comes from *Borovsky and Steinberg* [2006, also private communication, 2006]. As one aim of our study is to compare measured and modeled *Dst* indices, only CME- and CIR-driven storms having good solar wind data coverage were selected. In addition, we require that the storms be sufficiently, but not too strong, i.e., that during the 12 hours following storm onset, (1) the *Kp* index increases to a value of at least $4^+$, (2) the difference between the storm onset *Dst* value and the minimum *Dst* value is at least 40 nT, (3) there is neither obvious strong activity before the storm onset nor a large multiple peak main phase, and (4) the minimum *Dst* is in the range [−30, −150] nT. This last criterion is required to hold for the entire storm duration and comes from the fact that the *O'Brien and McPherron* [2000] model has been derived from the analysis of storms having minimum *Dst* values larger than −150 nT, and it is thus valid only in that range. The storm onset times were determined by visual inspection of the data (from the *Dst* and *VBz* values in particular). This set of criteria led to a total of 60 CME-driven storms for which the onset times are listed in Table 1. The set of 38 CIR-driven storms is listed in Table 2.

## 3. Results
## 3.1. Illustration From Two Selected CME-Driven Storms

[15] As the *Dst** model used in this study comes from a simple integration of equation (2) forward in time, the choice of the start time for integration may be critical. For consistency we begin the integration at a similar relative time for each storm. For every event in this study, the start time for the *Dst** model is taken to be 12 hours before the storm onset times listed in Tables 1 and 2. We construct the model *Dst** traces for the next 24 hours, i.e., taking into account the 12 first hours of the storm main phase. We then compare those to the measured *Dst** traces.

[16] Here we first illustrate the analysis and goal of the study by showing two sample CME-driven storm events.

**Table 1.** List of CME-Driven Storms Onset Times

| Year | $B_z$ | DOY[a] | Hour |
|------|-------|------|------|
| 1997 | N | 10 | 2 |
| 1997 | N | 40 | 16 |
| 1997 | N | 100 | 19 |
| 1997 | N | 111 | 10 |
| 1997 | S | 135 | 6 |
| 1997 | N | 215 | 14 |
| 1997 | N | 246 | 18 |
| 1997 | S | 283 | 17 |
| 1997 | S | 326 | 2 |
| 1997 | S | 364 | 2 |
| 1998 | S | 6 | 15 |
| 1998 | S | 29 | 21 |
| 1998 | N | 48 | 13 |
| 1998 | S | 84 | 8 |
| 1998 | S | 100 | 15 |
| 1998 | S | 122 | 9 |
| 1998 | N | 165 | 3 |
| 1998 | N | 176 | 22 |
| 1998 | N | 211 | 23 |
| 1998 | S | 218 | 2 |
| 1998 | N | 292 | 1 |
| 1998 | S | 311 | 11 |
| 1998 | S | 317 | 0 |
| 1999 | N | 23 | 15 |
| 1999 | N | 49 | 3 |
| 1999 | N | 106 | 19 |
| 1999 | S | 232 | 2 |
| 1999 | S | 347 | 2 |
| 2000 | S | 22 | 17 |
| 2000 | N | 61 | 3 |
| 2000 | S | 138 | 0 |
| 2000 | N | 144 | 22 |
| 2000 | N | 160 | 12 |
| 2000 | S | 175 | 17 |
| 2000 | S | 178 | 2 |
| 2000 | S | 195 | 11 |
| 2000 | N | 201 | 21 |
| 2000 | N | 205 | 13 |
| 2000 | S | 223 | 20 |
| 2000 | N | 278 | 4 |
| 2000 | N | 302 | 20 |
| 2000 | N | 331 | 18 |
| 2001 | S | 63 | 18 |
| 2001 | N | 86 | 19 |
| 2001 | N | 94 | 15 |
| 2001 | S | 98 | 13 |
| 2001 | S | 108 | 1 |
| 2001 | N | 112 | 1 |
| 2001 | N | 118 | 10 |
| 2001 | S | 148 | 9 |
| 2001 | N | 189 | 18 |
| 2001 | S | 229 | 12 |
| 2001 | S | 256 | 2 |
| 2001 | S | 304 | 19 |
| 2001 | N | 363 | 23 |
| 2002 | N | 59 | 19 |
| 2002 | N | 77 | 23 |
| 2002 | N | 82 | 14 |
| 2002 | N | 213 | 23 |
| 2002 | N | 230 | 21 |

[a]DOY, day of year.

The first CME occurred on 22 January 2000 and the second on 25 June 1998. The relevant data are shown in Figure 1 for each event, drawn in black and red, respectively, for 24 hours surrounding storm onset. Figure 1 shows the solar wind dynamic pressure ($P_{ram}$) (Figure 1a), the IMF magnitude (Figure 1b), the y component of the solar wind electric field ($VBz$) (Figure 1c), the IMF absolute clock angle (CA = $|\tan^{-1}(B_y/B_z)|$) (Figure 1d), the measured (solid) and modeled (dashed) $Dst^*$ index (Figure 1e), and the $Kp$ index (Figure 1f). The x axis corresponds to epoch time, in hours, relative to the storm onset.

[17] The two events were chosen for their clear difference in terms of the prevailing IMF direction prior to storm onset. Also, the other main parameters were quite similar during the first hours of the storm main phase ($VBz$ and $P_{ram}$ in particular). The 22 January 2000 event (black) corresponds to a case with steady horizontal IMF for more than 6 hours preceding storm onset, with an IMF absolute clock angle of CA $\sim 90°$ (Figure 1d). By contrast, the 25 June 1998 event (red) was preceded by a strong northward IMF (CA $\sim 30°$) for over 6 hours.

[18] For the 12 hours preceding the 22 January 2000 storm, the y component of the solar wind electric field ($E_y$) was slightly positive (Figure 1c), leading to a $Dst^*$ value of the order $-10$ to $-20$ nT. The $Dst^*$ value during the 12 hours preceding the 25 June 1998 was slightly higher (10–20 nT) owing to a negative $E_y$ (northward IMF). At storm onset, corresponding to a large increase in $E_y$, both cases show a large decrease in $Dst^*$. In terms of the model $Dst^*$, that decrease lasts for as long as the injection term in equation (2) is large enough to overcome the decay term. As $E_y$ resumes lower values more quickly during the main phase for the 25 June 1998 than for the 22 January 2000 event, both

**Table 2.** List of CIR-Driven Storms Onset Times

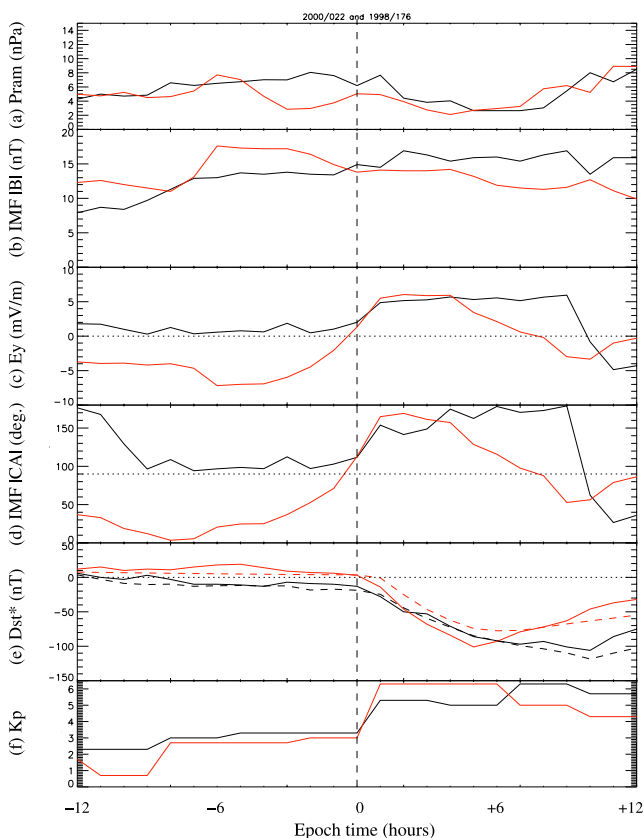| Year | $B_z$ | DOY | Hour |
|------|-------|-----|------|
| 1973 | N | 328 | 13 |
| 1974 | S | 25 | 2 |
| 1974 | S | 108 | 1 |
| 1974 | N | 122 | 22 |
| 1974 | S | 177 | 3 |
| 1974 | S | 203 | 23 |
| 1974 | S | 214 | 14 |
| 1974 | S | 315 | 11 |
| 1975 | S | 110 | 16 |
| 1975 | S | 136 | 5 |
| 1975 | N | 333 | 5 |
| 1976 | S | 58 | 13 |
| 1976 | S | 182 | 7 |
| 1977 | N | 67 | 19 |
| 1994 | S | 65 | 23 |
| 1995 | N | 29 | 2 |
| 1995 | N | 42 | 5 |
| 1995 | N | 68 | 18 |
| 1995 | S | 96 | 23 |
| 1995 | N | 122 | 2 |
| 1995 | N | 143 | 18 |
| 1995 | S | 197 | 13 |
| 1995 | S | 248 | 10 |
| 1995 | N | 303 | 11 |
| 1995 | S | 358 | 6 |
| 1999 | S | 269 | 15 |
| 1999 | S | 283 | 4 |
| 1999 | S | 311 | 4 |
| 2000 | S | 11 | 15 |
| 2000 | S | 36 | 17 |
| 2002 | S | 33 | 3 |
| 2002 | N | 36 | 16 |
| 2002 | S | 297 | 0 |
| 2002 | N | 324 | 16 |
| 2002 | S | 330 | 22 |
| 2003 | S | 191 | 23 |
| 2003 | N | 219 | 16 |
| 2003 | N | 233 | 0 |

**Figure 1.** Time series of solar wind and magnetospheric data for two CME-driven storms chosen for illustration on 22 January 2000 (black) and 25 June 1998 (red). (a) Dynamic pressure, (b) magnetic field magnitude, (c) y component of the solar wind electric field, (d) IMF absolute clock angle, (e) measured (solid lines) and modeled (dashed lines) $Dst^*$, and (f) $Kp$ index values. The onset time is given by the dashed vertical line. See text for further details.

the measured and modeled $Dst^*$ values start to increase 5–6 hours after storm onset for that event. On 22 January 2000 the $Dst^*$ values kept decreasing until the end of the 12 hour interval after storm onset owing to a more sustained positive $E_y$.

[19] The feature to note in Figure 1 is the fact that although the solar wind data for the two events appear similar during the first hours of the main phase, the model $Dst^*$ (red dashed lines in Figure 1e) underestimates the decrease in $Dst^*$ measured (red solid lines) for the main phase of the event preceded by northward IMF. The underestimation reaches about ∼30 nT at 5 hours after onset, corresponding to 30% of the measured $Dst^*$ value at that time. By contrast, the event preceded by horizontal IMF (black lines) is overall well reproduced by the model $Dst^*$.

## 3.2.  Analysis of CME-Driven Storms

[20] To search for a systematic discrepancy between the modeled and measured $Dst^*$ as a function of the prevailing IMF direction during the period preceding storm onset, we conduct a superposed epoch analysis of the set of CME-driven storms (Table 1). Figure 2 shows superposed epoch averages for the 24 hours surrounding storm onset for the 60

CME-driven storms. The 60 events were divided into two sets based on the preceding IMF conditions. In Figure 2, the black curves correspond to the superposed epoch averages of the parameters for events which have at most 1 hour (1 OMNI-2 data value) of IMF absolute clock angle CA < 60° (i.e., at most 1 hour of strong northward IMF) during the 6 hours preceding storm onset. The IMF preceding the storm is thus mainly horizontal or southward for these events. The total number of events fulfilling this criterion is 27 (out of 60). The red curves correspond to the superposed epoch averages from events which are preceded (within 6 hours) by at least two hours of IMF directed northward, defined as CA < 60°. Thirty-three events fulfill this criterion. In the following, we refer to the former type of events as "horizontal/southward IMF case" and to the latter as "northward IMF case." In Tables 1 and 2, the "N" (for northward) and "S"(for southward) notations in the Bz column refer to the subset of IMF preconditioning to which each event belongs to accord-
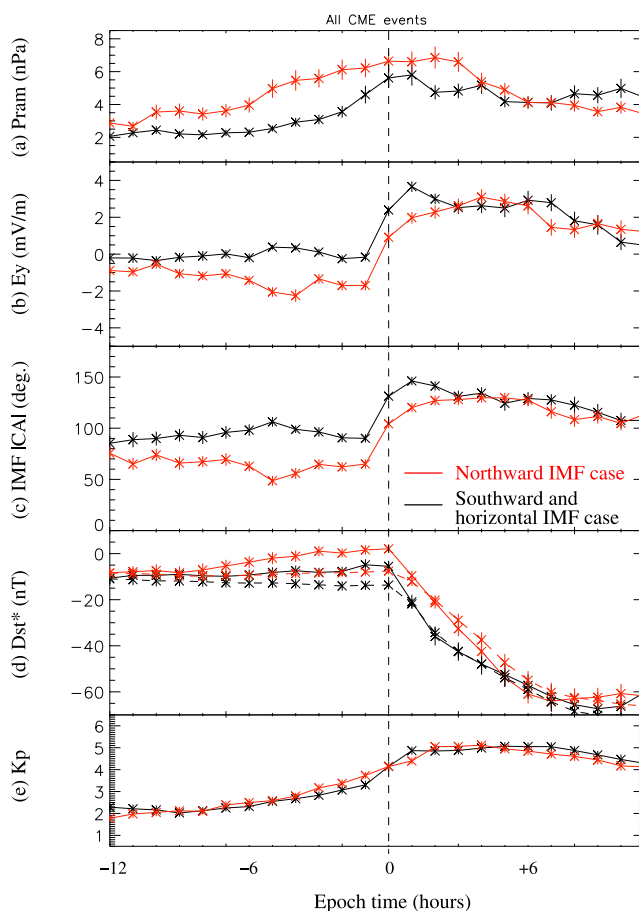


**Figure 2.** Superposed epoch time series of solar wind and magnetospheric data for the set of 60 CME-driven storms. The results for the 27 (33) events preceded by southward/horizontal (northward) IMF (see text for definitions) are shown with the black (red) lines. (a) Dynamic pressure, (b) y component of the solar wind electric field, (c) IMF absolute clock angle, (d) measured (solid lines) and modeled (dashed lines) $Dst^*$, and (e) $Kp$ index values. The onset time used for epoch superposition is shown by the dashed vertical line. See text for further details. Error bars show the mean absolute deviation of the mean.
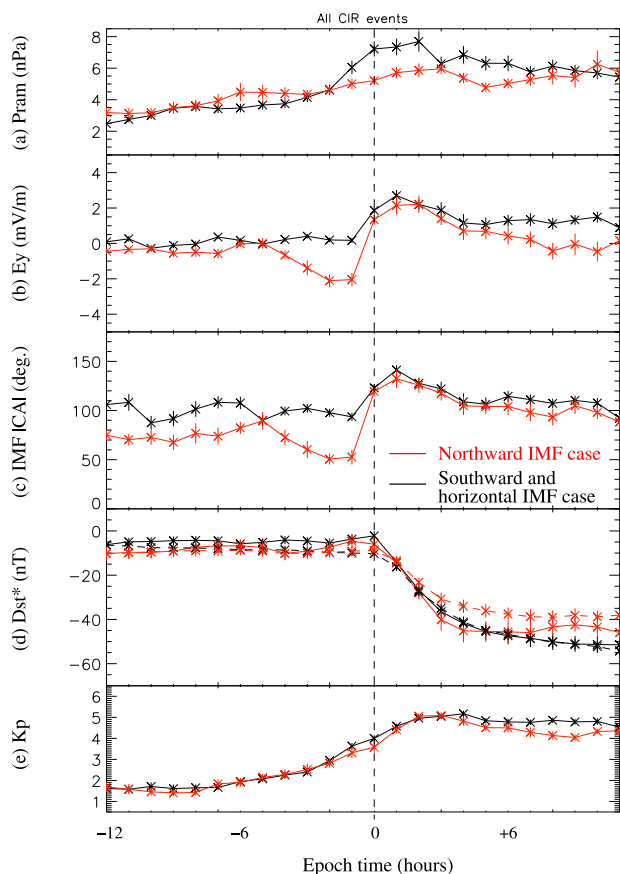
**Figure 3.** Superposed epoch time series of solar wind and magnetospheric data for the set of 38 CIR-driven storms. The results for the 24 (14) events preceded by southward/horizontal (northward) IMF (see text for definitions) are shown with the black (red) lines. This figure is in the same format as Figure 2.

ing to our selection criteria. The choice of a clock angle of 60° as a selection criterion comes from the fact that both double high-altitude reconnection and the Kelvin-Helmholtz instability may be effective in forming a cold, dense plasma sheet for such low clock angle values.

[21] In Figure 2, one observes that (1) the *Kp* values are similar for both sets of events (Figure 2e), (2) the *VBz* parameter (or $E_y$ in Figure 2b) and absolute IMF CA (Figure 2c) are more negative and lower, respectively, in the interval prior to storm onset for the events preceded by northward IMF, as a result of the selection criterion, and (3) after storm onset $E_y$ is somewhat larger in the case of the events preceded by horizontal/southward IMF. This latter characteristic is responsible for a faster (measured and modeled) *Dst** decrease in the first 2 hours following storm onset (Figure 2d). However, it appears that the overall decrease in measured *Dst** during the main phase of the storm is globally underestimated by the model in the case of events preceded by northward IMF (red curves). Indeed, compared to the model predictions, storms preceded by northward IMF appear to be stronger than those with no such preceding northward interval (Figure 2d). For the northward IMF case, the average underestimation is of ∼10 nT a few hours after storm onset. The observed difference is of the order of the average absolute deviation of the mean (i.e., the average absolute deviation from the mean

divided by the square root of the number of events) shown as the statistical error bars on both the measured and modeled *Dst**, and is therefore not dramatic. However, it corresponds to ∼15% of the average *Dst** at this time; this trend will be confirmed by the separate study of CIR-driven storms in section 3.3.

[22] It is worth noting that the correction (equation (1)) to remove the influence of the magnetopause current system does not seem to perform well generally. Figure 2a shows that the dynamic pressure of the solar wind ($P_{ram}$) is large for both sets of events. The discrepancy observed before storm onset between the modeled and measured *Dst** for both cases (Figure 2d) suggests that the pressure correction is not large enough. The discrepancy is slightly larger for the northward IMF cases (which have larger solar wind pressure associated with them). If an additional pressure correction were applied to the high-$P_{ram}$ main phase interval after onset, the corrected *Dst** would fall even further below the modeled value for the northward IMF case, therefore increasing the discrepancy for these conditions.

## 3.3. Analysis of CIR-Driven Storms

[23] Figure 3 presents the superposed epoch results from the analysis of the 38 CIR-driven storms listed in Table 2. The analysis performed and the event selection criteria are exactly the same as those used in the previous section for CME-driven storms. The format of Figure 3 is the same as Figure 2. The total number of events corresponding to the horizontal/southward (northward) IMF case is 24 (14) out of 38.

[24] In Figure 3, one again observes that (1) the *Kp* values (Figure 3e) are similar for both sets of events (horizontal/southward and northward IMF cases), (2) the *VBz* parameter (or $E_y$, Figure 3b) and absolute IMF CA (Figure 3c) are more negative and lower, respectively, in the interval prior to storm onset for the events preceded by northward IMF (red curves), again as a result of the selection criteria, and (3) after storm onset, $E_y$ is somewhat larger in the case of the events preceded by horizontal/southward IMF (black curves). In this case, this latter characteristic does not result in any clearly faster *Dst** decrease in the first hours following storm onset as far as the measured *Dst** is concerned (Figure 3d). The modeled *Dst** depends directly on this parameter (*VBz* or $E_y$), however, and it therefore decreases slightly faster for the horizontal/southward IMF case. As discussed for CME-driven storms in the previous section, a possible misrepresentation of the magnetopause current system correction may be indicated in Figure 3d as the slight difference between the modeled and observed *Dst** in the immediate prestorm hours.

[25] In terms of the general trends, for CIR-driven storms the model *Dst** again globally underestimates the decrease in measured *Dst** when the IMF has been northward in the 6 hours preceding storm onset. Compared to the model predictions, storms with preceding northward IMF intervals are stronger than those without (Figure 3d). The difference between the model and observations is even more significant than for the case of CME-driven storms when compared to the statistical error bars. The average underestimation is more than 10 nT for the northward IMF case a few hours after storm onset. It corresponds to ∼20% of the average *Dst** at this time. This separate study of CIR-driven storms thus confirms the global underestimation of the *Dst** magnitude
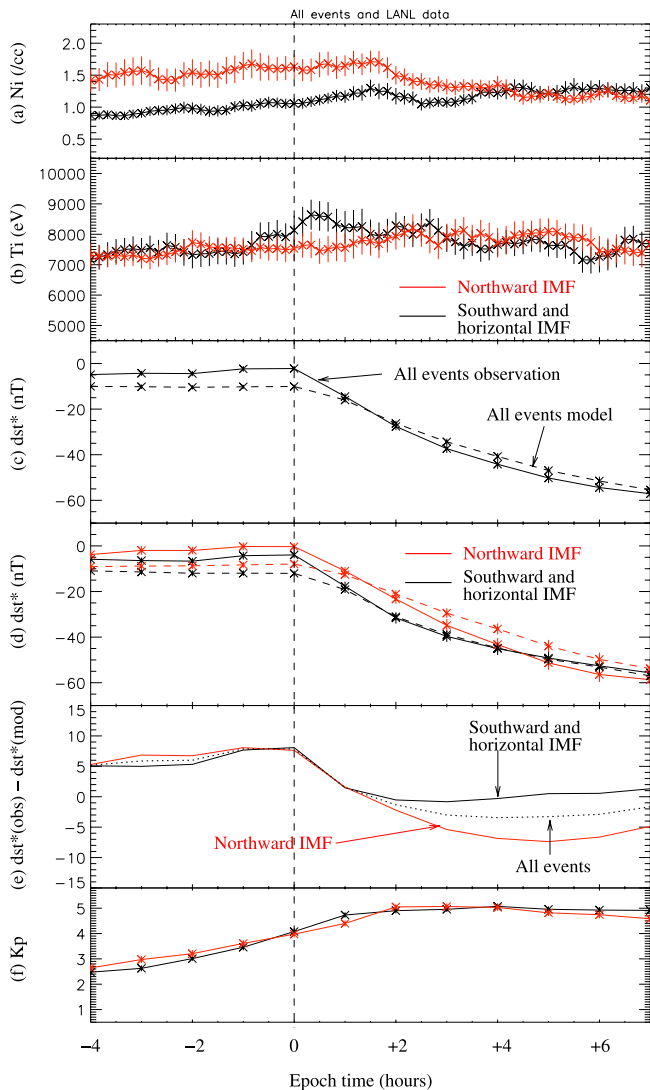
**Figure 4.** Superposed epoch time series of magnetospheric indices and geosynchronous data from the Los Alamos plasma instruments for the combined CME- and CIR-driven storms. The Los Alamos geosynchronous superposed time series are derived from the nightside measurements, as explained in the text. These data only come from the 84 (out of 98) events which occurred during the 1994–2003 period when the spacecraft were operative. The total set of 98 storms (60 CME and 38 CIR) is used for the indices ($Dst^*$, $Dst^*$ model and $Kp$) superposed time series. The results are separately shown for events preceded by southward/horizontal (black) and northward (red) IMF (see text for definitions), apart from Figure 4c that shows the $Dst^*$ traces for all events. (a) Geosynchronous densities, (b) geosynchronous temperatures, (c) measured (solid lines) and modeled (dashed lines) $Dst^*$ for all events, (d) measured (solid lines) and modeled (dashed lines) $Dst^*$ for southward/horizontal (black) and northward (red) IMF events, and (e) $Kp$ index values. The onset time used for epoch superposition is shown by the dashed vertical line. See text for further details. Error bars show the mean absolute deviation of the mean.

by the model when the IMF has been northward for a substantial interval before storm onset.

[26] We performed similar analyses using different criteria for the selection of northward IMF cases. The superposed epoch results for both CMEs and CIRs show a consistently larger $Dst^*$ magnitude than the model when one requires at least 3 and 4 hours of preceding northward IMF. Other analyses based on the IMF direction over the 12 hours preceding storm onset also confirmed this trend. This trend holds true when other sensible criteria are used for the definition of northward and horizontal/southward IMF cases.

[27] This underestimation of storm strength by the model may be attributed to additional physical processes not taken into account in the model formulation. We propose that such an additional coupling mechanism may be the occurrence of a preconditioning of the magnetosphere under northward IMF through the formation of a cold, dense plasma sheet in the midtail of the magnetosphere. To test this hypothesis, we study Los Alamos geosynchronous data for both sets of events in the next section. Geosynchronous spacecraft have previously been shown to constitute good monitors of plasma sheet access to the inner magnetosphere [*Korth et al.*, 1999; *Thomsen et al.*, 2003; *Denton et al.*, 2005; *Lavraud et al.*, 2005b].

### 3.4. Geosynchronous Data and Combined Results

[28] Figure 4 shows superposed epoch results for the combined set of CME- and CIR-driven storms, zoomed on the early storm main phase. The black and red curves (apart from Figure 4c) correspond to data from the set of events defined as horizontal/southward and northward IMF cases, respectively (Tables 1 and 2). Figures 4a and 4b show the ion density and temperature measured onboard Los Alamos geosynchronous spacecraft, sorted by preceding southward/horizontal (black) and northward (red) IMF. All available measurements during the time intervals of interest in the nightside region (1800–0600 LT) of geosynchronous orbit are used; the trends are similar when only considering measurements closer to midnight, but the statistics decrease. Figure 4c shows the superposed epoch averages of the measured (solid lines) and modeled (dashed lines) $Dst^*$ for all storms, without sorting by preceding IMF. Figure 4d shows the superposed epoch averages of the measured (solid lines) and modeled (dashed lines) $Dst^*$, sorted by preceding southward/horizontal (black) and northward (red) IMF. Figure 4e shows the superposed epoch averages of the difference between the measured and modeled $Dst^*$, sorted by preceding southward/horizontal (black) and northward (red) IMF, together with that for all events, i.e., without sorting by preceding IMF (dotted black line). Figure 4f shows the superposed epoch averages for the $Kp$ index, sorted by preceding southward/horizontal (black) and northward (red) IMF. Apart from 14 CIRs that occurred in the 1970s (Table 2), there are typically several geosynchronous spacecraft operative and contributing to the averages of Figures 4a and 4b. Figures 4c–4f show the results for all CMEs and CIRs, but those trends hold if the 14 CIRs from the 1970s are taken out of the averages.

[29] The global trends in the measured and modeled $Dst^*$ for the combined set of events follow those from the separate sets discussed earlier. Figure 4 shows that the model slightly underestimates storm strength when all events are taken into

account (Figure 4c) and that in the cases preceded by southward/horizontal IMF the model better reproduces the measured $Dst^*$ (Figure 4d). By contrast, the model underestimates even more the strength of storms preceded by northward IMF, which is made clear in Figure 4e were the difference between measured and modeled $Dst^*$ are shown. The reason why the model underestimates the strength of storms when all events are taken into account is unclear. It may come from the fact that the model of *O'Brien and McPherron* [2000] was not constructed based on the present set of storms. In a relative sense, however, it is clear that the model $Dst^*$ globally tends to underestimate the ring current strength during the main phase of storms that have been preceded by a substantial interval of northward IMF. Note that we have performed this analysis using start times, for integration of the Burton formula, closer to the storm onset time (i.e., less than 12 hours), and the results confirmed the relative underestimation (by similar amounts) of the storm strength for events preceded by northward IMF. The underestimation attains $\sim 5-10$ nT which is $\sim 10-20\%$ of the $Dst^*$ value at that time. For isolated cases with strong and sustained northward IMF preceding the storm, such as for the north-south polarity magnetic cloud of 25 June 1998 in Figure 1, the underestimation may even be greater (e.g., 30%). Although the trend observed in the present study appears systematic (observed for different sets of events), the error bars associated with them are of the order of the difference itself. Therefore additional studies will be required to further confirm and constrain this tendency when larger CME and CIR sets are available.

[30] Los Alamos data in Figures 4a and 4b show a clear tendency for the plasma sheet accessing geosynchronous orbit in the midnight sector around storm onset to have a much larger density and a slightly lower temperature in the case of storms preceded by intervals of northward IMF than in the case of storms preceded by horizontal/southward IMF. This ensemble of results is compatible with the hypothesis that a preceding northward IMF interval leads to the formation of a cold, dense plasma sheet (CDPS), which in turn is pushed inward by the increased convection at storm onset. This larger plasma sheet density seems to lead to a larger ring current than a more tenuous plasma sheet for similar solar wind driving conditions (within error uncertainties), as was suggested in the study by *Thomsen et al.* [1998] and several simulation studies [*Jordanova et al.*, 1998; *Kozyra et al.*, 1998]. The colder nature of the plasma sheet also has a potential geoeffective role, as colder plasma can be convected further inward than hot plasma that curvature and gradient drifts more readily out of the ring current region [*Ebihara and Ejiri*, 2000].

## 3.5. Discussion

[31] In this section, we discuss the results and associated potential limiting factors in relation with the preconditioning mechanism presented in this paper. These pertain to (1) limitations due to statistical aspects and data availability, (2) the effects from the magnetopause current system and solar wind dynamic pressure, (3) the contribution of ionospheric plasma to the ring current, (4) the removal/expulsion of part of the plasma sheet from the magnetotail at storm onset, and (5) the mass loading of dayside reconnection (and

convection) owing to the formation of a plasmasphere under northward IMF.

[32] The survey of the individual events constituting the data set used in this study revealed that a majority of CMEs and CIRs are preceded by relatively variable conditions, including that in magnetic field direction. To address the topic of this paper, we have used the criteria which we thought most sensible (see section 3.2). However, the effects of variable IMF direction, in particular, on the formation of the cold, dense plasma sheet could not be assessed thoroughly. In the future, this mechanism ought to be studied by use of more extended data sets, out of which significant lists of events with preceding steady conditions may be identified; i.e., in order to fully isolate the effect sought in the present paper.

[33] An interesting result regarding the Burton formulation is seen in all figures plotting the modeled and observed pressure-corrected $Dst^*$. It appears that prior to the storm, the pressure correction is not sufficient to account for the measured $Dst^*$, and thus the measured values in all cases lie above the modeled ones. This discrepancy is quickly recovered as the activity increases at storm onset. As one interpretation, it is noted that *Siscoe et al.* [2005] recently discussed the dependence of the pressure correction on the driving electric field. They concluded that the correction is largest for lowest levels of the driving electric field and goes to almost zero as the driving electric field reaches values close to 10 mV/m. If such a $VBz$ dependence was adopted, this would tend to reduce the pressure correction after the storm onset. However, as the changes to the model and observations would be similar in both preconditioning cases, it appears that our conclusions would remain unchanged. Also, concerning the Burton formulation, we wish to point out that the parameterization performed by *O'Brien and McPherron* [2000] was made statistically using data from both quiet and active times.

[34] Large ring current development is associated with large-scale magnetospheric and ionospheric disturbances. During such active times, the ionosphere supplies the plasma sheet with large amounts of material, out of which $O^+$ ions have been shown to contribute most [e.g., *Young et al.*, 1982; *Lennartsson*, 1995; *Nosé et al.*, 2003]. Therefore, although the solar wind is known to be an important source of plasma for the plasma sheet (and in turn the ring current), the contribution of $O^+$ ions to the plasma sheet density and to the ring current strength has been shown to be important (and sometimes dominant) [*Hamilton et al.*, 1988; *Daglis et al.*, 1993; *Daglis*, 1997]. Therefore a potential masking factor to the preconditioning mechanism discussed here comes from the fact that the solar wind (implying the cold, dense plasma sheet) is not the sole source of material for the ring current. However, the timings of the two effects are different: while the preconditioning takes place during the hours prior to the onset, and hence affects the storm early main phase, the increase in the ionospheric outflow and especially oxygen outflow is enhanced only as the level of activity increases toward the peak of the main phase. Thus, even assuming that $Dst$ carries a signature from the ionospheric outflows, the conclusions about the preconditioning effect discussed here remain unchanged.

[35] The onset of enhanced convection that transports the plasma sheet toward geosynchronous orbit and the ring

current also leads to magnetic reconnection in the midtail, which would result in the (tailward) expulsion of the plasma sheet located tailward of the reconnection line. Thus, even when preconditioning by northward IMF occurs, only a limited portion of the tail CDPS is transported to the inner magnetosphere. In other words, the denser plasma of the CDPS may constitute a source for the ring current only in the early stage of the main phase, after which it may be replaced by fresh plasma that has different characteristics. Substorms or other processes associated with midtail reconnection would thus cut the supply of cold and dense plasma (CDPS) to the inner magnetosphere and therefore limit the effects of this preconditioning mechanism. From Figure 4a denser plasma sheet is detected at geosynchronous orbit for $2-4$ hours following storm onset in the northward IMF case. This constitutes a lower timescale limit to the influence of the CDPS on the ring current, which is located deeper inside geosynchronous orbit. Exact timescales for this process will be determined in future work from comparisons with ring current models.

[36] Finally, recent works have suggested [*Borovsky and Steinberg*, 2006; *Borovsky and Denton*, 2006] that the formation of a dense plasmasphere during northward IMF may in turn lower the dayside reconnection rate (e.g., as indicated by the Polar Cap Index), by decreasing the Alfvén speed near the reconnection site, after an increase in convection has led to the formation of a plasmaspheric plume on the dayside. This scenario also constitutes a preconditioning of the magnetosphere under northward IMF (quiet conditions are also conducive to the formation of a plasmasphere). If one presumes that dayside reconnection influences global convection, and indirectly the strength of storms, this mechanism would be counteracting the preconditioning mechanism due to the formation of a cold, dense plasma sheet (CDPS). However, in the context of the present study, the fact that the $Kp$ values for northward and southward/horizontal IMF cases in Figure 4f closely follow each other suggests that the present results (for our set of events) are independent of this other mechanism.

## 4. Conclusion

[37] We have studied the possible preconditioning effect of the IMF history on the geoeffectiveness of both CMEs (60 events) and CIRs (38 events). We have analyzed the magnetospheric response to those two types of solar wind structures (1) in terms of both measured and modeled $Dst$* index and (2) in terms of the associated geosynchronous observations of the density and temperature of the plasma sheet accessing the inner magnetosphere at storm onset. We first focused on the difference between measured and modeled [*Wang et al.*, 2003] $Dst$* signatures during those events. We have shown that, for both cases separately as well as combined, the model $Dst$* tends to underestimate the actual storm strength for events that are preceded by northward IMF intervals. Although the differences observed are of the order of the error bars, this trend was confirmed separately for the two sets of storms, i.e., CME- and CIR-driven storms. The average underestimation is of the order of $5-10$ nT, which corresponds to $10-20\%$ of the average $Dst$* value for these events. This result suggests that, for similar solar wind electric field and dynamic pressure profiles, CME or CIR

structures that are preceded by strongly northward IMF are more geoeffective than those preceded by horizontal/southward IMF. An example is the storm driven by the north-south polarity magnetic cloud on 25 June 1998, which shows an underestimation of $\sim30\%$ in the magnitude of $Dst$*.

[38] We further analyzed the available Los Alamos geosynchronous data for the events under consideration and demonstrated that the plasma sheet density and temperature in the midnight sector around storm onset are significantly larger and slightly lower, respectively, for the events preceded by northward IMF intervals. This fact shows the presence of a colder and denser plasma sheet before storm onset in the midtail region and formed under the prevailing northward IMF conditions. This cold, dense plasma sheet apparently is conducive of an increased ring current owing to potentially both its larger density and colder nature. The formation of a cold, dense plasma sheet under northward IMF thus seems to precondition the magnetosphere by leading to the creation of a stronger ring current during the early main phase of the ensuing storm.

[39] These results highlight the necessity for further studies of this, as well as other, potential preconditioning processes. Future models need to better represent the effects of such preconditioning mechanisms through the addition of appropriate formulations in the $Dst$ models. The current number of CME and CIR events of substantial strength and with good solar wind data coverage (and steady preceding conditions) may not be extensive enough to perform such a task. However, the fact that north-south polarity magnetic clouds are expected to become prevalent during solar cycle 24 starting in 2007 [*Mulligan et al.*, 1998; *Li and Luhmann*, 2004] may enable us (1) to further confirm, (2) to better quantify this mechanism, and (3) to potentially implement it in more elaborate schemes [e.g., *Temerin and Li*, 2002] of $Dst$ prediction.

## References

Akasofu, S.-I. (1981), Energy coupling between the solar wind and the magnetosphere, *Space Sci. Rev.*, *28*, 121–190.
Bame, S. J., D. J. McComas, M. F. Thomsen, B. L. Barraclough, R. C. Elphic, J. P. Glore, J. T. Gosling, J. C. Chavez, E. P. Evans, and J. F. Wymer (1993), Magnetospheric plasma analyzer for spacecraft with restrained resources, *Rev. Sci. Instrum.*, *64*(4), 1026–1033.
Borovsky, J. E., and M. H. Denton (2006), Effect of plasmaspheric drainage plumes on solar-wind/magnetosphere coupling, *Geophys. Res. Lett.*, doi:10.1029/2006GL026519, in press.
Borovsky, J. E., and J. T. Steinberg (2006), The "calm before the storm" in CIR/magnetosphere interactions: Occurrence statistics, solar wind statistics, and magnetospheric preconditioning, *J. Geophys. Res.*, *111*, A07S10, doi:10.1029/2005JA011397.
Borovsky, J. E., M. F. Thomsen, and D. J. McComas (1997), The superdense plasma sheet: Plasmaspheric origin, solar wind origin, or ionospheric origin?, *J. Geophys. Res.*, *102*(A10), 22,089–22,102.
Burton, R. K., R. L. McPherron, and C. T. Russell (1975), An empirical relationship between interplanetary conditions and *Dst*, *J. Geophys. Res.*, *80*(31), 4204–4214.
Cane, H. V., and I. G. Richardson (2003), Interplanetary coronal mass ejections in the near-Earth solar wind during 1996–2002, *J. Geophys. Res.*, *108*(A4), 1156, doi:10.1029/2002JA009817.
Daglis, I. A. (1997), The role of magnetosphere-ionosphere coupling in magnetic storm dynamics, in *Magnetic Storms*, *Geophys. Monogr. Ser.*, vol. 98, edited by B. T. Tsurutani et al., pp. 107–116, AGU, Washington, D. C.

Daglis, I. A., E. T. Sarris, and B. Wilken (1993), AMPTE/CCE CHEM observations of the ion population at geosynchronous altitudes, *Ann. Geophys.*, *11*, 685–696.

Denton, M. H., M. F. Thomsen, H. Korth, S. Lynch, J.-C. Zhang, and M. W. Liemohn (2005), Bulk plasma properties at geosynchronous orbit, *J. Geophys. Res.*, *110*, A07223, doi:10.1029/2004JA010861.

Denton, M. H., J. E. Borovsky, R. M. Skoug, M. F. Thomsen, B. Lavraud, M. G. Henderson, R. L. McPherron, J. C. Zhang, and M. W. Liemohn (2006), Geomagnetic storms driven by ICME- and CIR-dominated solar wind, *J. Geophys. Res.*, *111*, A07S07, doi:10.1029/2005JA011436.

Ebihara, Y., and M. Ejiri (2000), Simulation study on fundamental properties of the storm-time ring current, *J. Geophys. Res.*, *105*(A7), 15,843–15,859.

Fenrich, F. R., and J. G. Luhmann (1998), Geomagnetic response to magnetic clouds of different polarity, *Geophys. Res. Lett.*, *25*(15), 2999–3002.

Fujimoto, M., T. Terasawa, T. Mukai, Y. Saito, T. Yamamoto, and S. Kokubun (1998), Plasma entry from the flanks of the near-Earth magnetotail: Geotail observations, *J. Geophys. Res.*, *103*(A3), 4391–4408.

Ganushkina, N. Y., T. I. Pulkkinen, M. V. Kubyshkina, H. J. Singer, and C. T. Russell (2004), Long-term evolution of magnetospheric current systems during storm periods, *Ann. Geophys.*, *22*(4), 1317–1334.

Gonzalez, W. D., B. T. Tsurutani, R. P. Lepping, and R. Schwenn (2002a), Interplanetary phenomena associated with very intense geomagnetic storms, *J. Atmos. Sol. Terr. Phys.*, *64*(2), 173–181.

Gonzalez, W. D., B. T. Tsurutani, and A. L. Clua de Gonzalez (2002b), Geomagnetic storms contrasted during solar maximum and near solar minimum, *Adv. Space Res.*, *30*(10), 2301–2304.

Gosling, J. T. (1993), The solar flare myth, *J. Geophys. Res.*, *98*(A11), 18,937–18,949.

Gosling, J. T., D. J. McComas, J. L. Phillips, and S. J. Bame (1991), Geomagnetic activity associated with Earth passage of interplanetary shock disturbances and coronal mass ejections, *J. Geophys. Res.*, *96*(A5), 7831–7839.

Hakkinen, L. V. T., T. I. Pulkkinen, R. J. Pirjola, H. Nevanlinna, E. I. Tanskanen, and N. E. Turner (2003), Seasonal and diurnal variation of geomagnetic activity: Revised *Dst* versus external drivers, *J. Geophys. Res.*, *108*(A2), 1060, doi:10.1029/2002JA009428.

Hamilton, D. C., G. Gloeckler, F. M. Ipavich, W. Stüdemann, B. Wilken, and G. Kremser (1988), Ring current development during the great geomagnetic storm of February 1986, *J. Geophys. Res.*, *93*, 14,343–14,355.

Hasegawa, H., et al. (2004), Rolled-up Kelvin-Helmholtz vortices and associated solar wind entry at Earth's magnetopause, *Nature*, *430*, 755–758.

Huttunen, K. E. J., H. E. J. Koskinen, and R. Schwenn (2002), Variability of magnetospheric storms driven by different solar wind perturbations, *J. Geophys. Res.*, *107*(A7), 1121, doi:10.1029/2001JA900171.

Jordanova, V. K., C. J. Farrugia, L. Janoo, J. M. Quinn, R. B. Torbert, K. W. Ogilvie, R. P. Lepping, J. T. Steinberg, D. J. McComas, and R. D. Belian (1998), October 1995 magnetic cloud and accompanying storm activity: Ring current evolution, *J. Geophys. Res.*, *103*(A1), 79–92.

Kamide, Y., et al. (1998), Current understanding of magnetic storms: Storm-substorm relationships, *J. Geophys. Res.*, *103*(A8), 17,705–17,728.

King, J. H., and N. E. Papitashvili (2005), Solar wind spatial scales in and comparisons of hourly Wind and ACE plasma and magnetic field data, *J. Geophys. Res.*, *110*(A2), A02209, doi:10.1029/2004JA010804.

Korth, H., M. F. Thomsen, J. E. Borovsky, and D. J. McComas (1999), Plasma sheet access to geosynchronous orbit, *J. Geophys. Res.*, *104*(A11), 25,047–25,062.

Kozyra, J. U., V. K. Jordanova, J. E. Borovsky, M. F. Thomsen, D. J. Knipp, D. S. Evans, D. J. McComas, and T. E. Cayton (1998), Effects of a high-density plasma sheet on ring current development during the November 2–6, 1993, magnetic storm, *J. Geophys. Res.*, *103*(A11), 26,285–26,306.

Lavraud, B., et al. (2005a), Characteristics of the magnetosheath electron boundary layer under northward IMF: Implications for high-latitude reconnection, *J. Geophys. Res.*, *110*, A06209, doi:10.1029/2004JA010808.

Lavraud, B., M. H. Denton, M. F. Thomsen, J. E. Borovsky, and R. H. W. Friedel (2005b), Superposed epoch analysis of dense plasma access to geosynchronous orbit, *Ann. Geophys.*, *23*(7), 2519–2529.

Lavraud, B., M. F. Thomsen, B. Lefebvre, S. J. Schwartz, K. Seki, T. D. Phan, Y. L. Wang, A. N. Fazakerley, H. Rème, and A. Balogh (2006), Evidence for newly closed magnetosheath field lines at the dayside mag-

netopause under northward IMF, *J. Geophys. Res.*, *111*, A05211, doi:10.1029/2005JA011266.

Lennartsson, O. W. (1995), Statistical investigation of IMF $B_z$ effects on energetic (0.1- to 16-keV) magnetospheric $O^+$ ions, *J. Geophys. Res.*, *100*(A12), 23,621–23,636.

Li, W. H., et al. (2005), Plasma sheet formation during long period of northward IMF, *Geophys. Res. Lett.*, *32*, L12S08, doi:10.1029/2004GL021524.

Li, Y., and J. Luhmann (2004), Solar cycle control of the magnetic cloud polarity and the geoeffectiveness, *J. Atmos. Sol. Terr. Phys.*, *66*(3/4), 323–331.

McComas, D. J., S. J. Bame, B. L. Barraclough, J. R. Donart, R. C. Elphic, J. T. Gosling, M. B. Moldwin, K. R. Moore, and M. F. Thomsen (1993), Magnetospheric Plasma Analyzer: Initial three-spacecraft observations from geosynchronous orbit, *J. Geophys. Res.*, *98*, 13,453–13,465.

Mulligan, T., C. T. Russell, and J. G. Luhmann (1998), Solar cycle evolution of the structure of magnetic clouds in the inner heliosphere, *Geophys. Res. Lett.*, *25*(15), 2959–2962.

Nosé, M., R. W. McEntire, and S. P. Christon (2003), Change of the plasma sheet ion composition during magnetic storm development observed by the Geotail spacecraft, *J. Geophys. Res.*, *108*(A5), 1201, doi:10.1029/2002JA009660.

O'Brien, T. P., and R. L. McPherron (2000), An empirical phase space analysis of ring current dynamics: Solar wind control of injection and decay, *J. Geophys. Res.*, *105*(A4), 7707–7719.

Øieroset, M., J. Raeder, T. D. Phan, S. Wing, J. P. McFadden, W. Li, M. Fujimoto, H. Rème, and A. Balogh (2005), Global cooling and densification of the plasma sheet during an extended period of purely northward IMF on October 22–24, 2003, *Geophys. Res. Lett.*, *32*, L12S07, doi:10.1029/2004GL021523.

Siscoe, G. L., R. L. McPherron, and V. K. Jordanova (2005), Diminished contribution of ram pressure to *Dst* during magnetic storms, *J. Geophys. Res.*, *110*, A12227, doi:10.1029/2005JA011120.

Song, P., and C. T. Russell (1992), Model of the formation of the low-latitude boundary layer for strongly northward interplanetary magnetic field, *J. Geophys. Res.*, *97*(A2), 1411–1420.

Temerin, M., and X. Li (2002), A new model for the prediction of *Dst* on the basis of the solar wind, *J. Geophys. Res.*, *107*(A12), 1472, doi:10.1029/2001JA007532.

Terasawa, T., et al. (1997), Solar wind control of density and temperature in the near-Earth plasma sheet: WIND/GEOTAIL collaboration, *Geophys. Res. Lett.*, *24*(8), 935–938.

Thomsen, M. F., J. E. Borovsky, D. J. McComas, and M. R. Collier (1998), Variability of the ring current source population, *Geophys. Res. Lett.*, *25*(18), 3481–3484.

Thomsen, M. F., E. Noveroske, J. E. Borovsky, and D. J. McComas (1999), Calculation of moments from measurements by the Los Alamos magnetospheric plasma analyzer, *LA Rep. LA-13566-MS*, Los Alamos Natl. Lab., Los Alamos, N. M.

Thomsen, M. F., J. E. Borovsky, R. M. Skoug, and C. W. Smith (2003), Delivery of cold, dense plasma sheet material into the near-Earth region, *J. Geophys. Res.*, *108*(A4), 1151, doi:10.1029/2002JA009544.

Wang, C. B., J. K. Chao, and C.-H. Lin (2003), Influence of the solar wind dynamic pressure on the decay and injection of the ring current, *J. Geophys. Res.*, *108*(A9), 1341, doi:10.1029/2003JA009851.

Wu, C.-C., and R. P. Lepping (2002), Effects of magnetic clouds on the occurrence of geomagnetic storms: The first 4 years of Wind, *J. Geophys. Res.*, *107*(A10), 1314, doi:10.1029/2001JA000161.

Wu, C.-C., and R. P. Lepping (2005), Relationships for predicting magnetic cloud-related geomagnetic storm intensity, *J. Atmos. Sol. Terr. Phys.*, *67*(3), 283–291.

Young, D. T., H. Balsiger, and J. Geiss (1982), Correlations of magnetospheric ion composition with geomagnetic and solar activity, *J. Geophys. Res.*, *87*(A11), 9077–9096.

Zhang, G., and L. F. Burlaga (1988), Magnetic clouds, geomagnetic disturbances, and cosmic-ray decreases, *J. Geophys. Res.*, *93*(A4), 2511–2518.

————————————

J. E. Borovsky, M. H. Denton, B. Lavraud, T. I. Pulkkinen, and M. F. Thomsen, Space Science and Applications, MS D466, Los Alamos National Laboratory, Los Alamos, NM 87545, USA. (lavraud@lanl.gov)